

Estimation of keyhole geometry and prediction of welding defects during laser welding based on a vision system and a radial basis function neural network

Masiyang Luo¹ · Yung C. Shin¹

Received: 30 May 2014 / Accepted: 23 March 2015 / Published online: 6 May 2015
© Springer-Verlag London 2015

Abstract In keyhole welding, welding quality is closely related to the stability of the keyhole, which is primarily determined by keyhole geometry during the welding process. Three essential attributes to describe the simplified three-dimensional keyhole shape include keyhole size, penetration depth, and keyhole inclination angle. However, when using traditional measurement techniques, it is very challenging to take in-process measurements of penetration depth and inclination angle, even if the keyhole size can be detected by using a visual monitoring system. To realize the on-line estimation of keyhole dynamics and welding defects, a data-based radial basis function neural network state observer is adopted for estimating penetration depth and inclination angle in the transient state when welding parameters change suddenly. First, a static neural network is trained in advance to establish a correlation between the welding parameters and unobservable keyhole geometry. The dynamic state observer is trained based on the transient welding conditions predicted by a numerical model and then used to estimate the time-varying keyhole geometry. Meanwhile, a coaxial monitoring system is used to observe the keyhole shape from the top side in real time, which not only provides input to the neural network but also indicates the potential welding porosities. The predicted results are validated by experimental data obtained by welding of stainless steel 304 and magnesium alloy AZ31B.

Keywords Laser keyhole welding · Keyhole dynamics estimation · Radial basis function neural network · Coaxial monitoring · Porosity detection

✉ Yung C. Shin
shin@ecn.purdue.edu

¹ Center for Laser-Based Manufacturing, School of Mechanical Engineering, Purdue University, West Lafayette, IN 47907, USA

1 Introduction

All laser welding techniques can be classified into two basic categories: keyhole or conduction welding. Keyhole, or deep-penetration welding, is probably the most popular welding form. In keyhole welding, vapor pressure holds back the surrounding molten metal and keeps this hole open during the process. The metal vapor also scatters the laser beam into the molten metal along the side of the keyhole, thus transferring energy through the entire depth of the keyhole, resulting in a weld with a high aspect ratio, as illustrated in Fig. 1.

To ascertain the keyhole dynamics, especially the keyhole shape during deep-penetration welding, much research has been conducted on the modeling of keyhole changes in terms of different physical assumptions. Matsunawa and Semak [1] developed a simulation model of the front keyhole wall behavior on the basis of a hydrodynamic model that assumed that only the front part of the keyhole wall is exposed to the high-intensity laser beam and the growth of the keyhole wall inside the material is due to melt expulsion. To obtain a better understanding of the keyhole geometry, Lankalapalli et al. [2] developed a model for estimating penetration depth based on a two-dimensional heat conduction model and a conical keyhole assumption. Ronda et al. [3] investigated the relationship between the shape of the keyhole, surface tension, and a recoil force based on numerical simulation. However, these simplified models may not be able to accurately reflect the real dynamic changes of the keyhole. Ki et al. [4, 5] developed more complicated and well-considered models based on level-set equations. Pang et al. [6] proposed a three-dimensional sharp interface model, which combined three-dimensional heat transfer, keyhole free surface evolutions, and fluid flow in the welding process. In this model, not only the keyhole wall but also periodical keyhole collapse and bubble formation processes could be simulated successfully. Another model considering plasma gas, liquid metal, and solid metal was

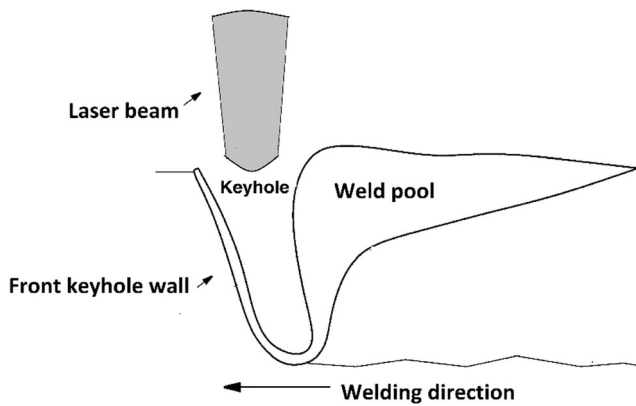


Fig. 1 Schematic of keyhole welding

proposed to describe the keyhole phenomena of laser welding [7]. Lately, a multi-phase numerical simulation based on the level-set model and a sharp interface model was used to accurately capture the dynamics of the keyhole, the molten pool, and even the plume [8].

Although the various numerical models are capable of describing the transient keyhole shape, they cannot be used for real-time applications due to their high computational requirements. Because of the great amount of data required for keyhole analysis and unavoidable time and cost, other studies focusing on keyhole dynamics have been carried out through multiple experimental observation techniques.

To monitor the welding process, many detecting systems have been developed based on different measurement techniques, such as acoustic, infrared, and imaging signals. Li et al. [9] used the “acoustic mirror” to investigate the ultrasonic airborne acoustic emission of the weld pool plasma and laser beam. Wang et al. [10] and Huang et al. [11] measured welding temperature distributions by an IR thermography system. At present, since the development of visual imaging techniques and high computational capability with a reduction of cost, a vision-based system has become a very popular technique to monitor the weld pool. Measurements have been conducted using a high-speed camera and a dot matrix pattern laser so as to reconstruct the three-dimensional weld pool surface in gas tungsten arc welding (GTAW) [12, 13]. Kim et al. [14] investigated the size of keyhole and Zhang et al. [15] extracted molten pool edges by using coaxial monitoring systems.

A high-speed camera-based vision system has been developed by Fabbro et al. [16–18] to learn the keyhole behavior in full-penetration laser welding. The penetration depth and keyhole front tilting angle were two significant areas of focus in this study. The related keyhole dynamic models were also introduced to validate their experimental results. A study at Osaka University incorporated more complicated measurement techniques, utilizing high-speed video cameras and an X-ray transmission real-time imaging system to investigate the dynamic phenomena inside the keyhole and the weld pool on different materials, such as

Table 1 Description of IPG YLS-1000 fiber laser

Available output power	≤1000 W
Emission wavelength	1070–1080 nm
Diameter of feed fiber	200 μm
Dope material	Ytterbium
Wall-plug efficiency	<30 %

stainless steel and magnesium alloy [19, 20]. In the process of deep-penetration laser welding, due to the high energy density of the heat input source on the workpiece, the material evaporates rapidly and the formed keyhole is unstable. As the liquid flow is very complicated and the keyhole geometry fluctuates frequently under some welding conditions, this would influence the quality and performance of the welding joint. For instance, the bubbles formed from keyhole collapse and shrinkage cause the keyhole-induced porosity. Based on the X-ray imaging system, the formation of bubbles and welding porosities could also be captured in real time [21–23]. However, the high cost of the whole system and overly complicated imaging signals of the keyhole make this monitoring system unsuitable for implementation as a real welding process control system.

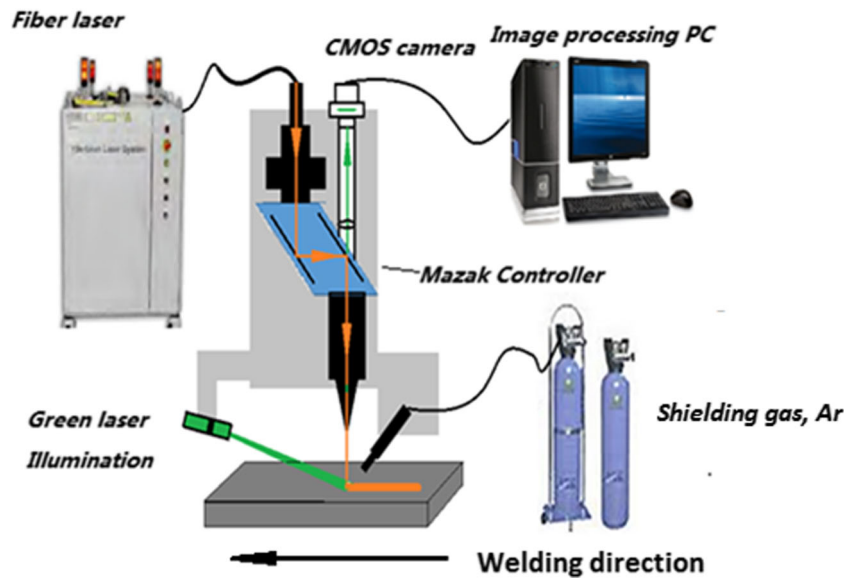
In this work, a coaxial monitoring system is developed to detect the keyhole shape from the top side. To approximate the keyhole dynamics in more straightforward and efficient manner under different welding conditions, a data-based static radial basis function neural network (RBFNN) is trained in order to establish the relationship among different welding parameters, system measurements, and unobservable keyhole dynamics. Further, a dynamic RBFNN identification method [24, 25] is used to estimate the penetration depth and keyhole front tilting angle for the transient state welding when some welding conditions change suddenly. The purpose of using this observer is to estimate the change of weld pool geometry due to unknown reasons, such as the nonuniformity of work material and absorptivity changes. The data-based RBFNN could be trained based on experimental data and modeling results in advance so that it could be implemented as a state observer to provide sufficient feedback of keyhole dynamics during the laser welding process in real time. Lastly, based on the visual monitoring system, two approaches are proposed to estimate in-process welding porosities.

The remainder of the paper is organized as follows: Section 2 describes the experimental setup of the coaxial visual monitoring system, while the third section presents the methodology of using the static RBFNN and the dynamic

Table 2 Chemical composition of stainless steel 304

Element	C	Mn	P	S	Si	Cr	Ni	N	Fe
Portion (%)	0.08	2	0.045	0.03	0.75	10	10	0.1	Balance

Fig. 2 Coaxial visual monitoring system



observer used to predict keyhole dynamics. The fourth section of the paper contains the actual implementation results with the RBFNN based on experimental data and the mechanism of porosity predictions. The final section concludes the paper.

2 Experimental setup

In this work, the keyhole welding process is performed by a fiber laser (IPG photonics YLS-1000, details of which are shown in Table 1) with a focal diameter of 200 μm . The laser beam is transmitted through the fiber to the laser head and its wavelength is 1070 nm. Stainless steel 304 with a thickness of 2 mm is used as the substrate material; its chemical composition is listed in Table 2. Argon is used as a shielding gas and blown into the weld pool to improve the weldment quality in the experiments. A three-axis open-architecture controlle integrated with a MAZAK machining center is utilized to control the welding process.

To observe the keyhole from the top side, a coaxial vision-based monitoring system was designed. The coaxial monitoring system is composed of two dichroic mirrors, a complementary metal-oxide-semiconductor (CMOS) camera (DFK

42BUC03), an illumination source, and optic filters. The entire monitoring system and the laser head are all mounted on the Mazak CNC machine. Two dichroic mirrors are set parallel to each other into a parallelogram block so that the output beam can be perfectly focused on the base material, as schematically shown in Fig. 2.

Both the dichroic mirrors completely reflect the laser beam around the wavelength of 1070 nm but transmit others, which makes it possible to capture the weld pool images through the illumination at different wavelengths. The preset resolution of the camera is 1280×720 pixels with a maximum frame speed of 33 frames/s.

To efficiently reduce the impact of disturbing imaging noises of the plume and plasma that come out from the key-hole, a 200-mW focus-adaptable green laser with the wavelength close to 530 nm was selected as the illuminant after the spectrum analysis of the weld pool. The illuminating area was adjusted to cover the entire weld pool region. In addition, a narrow band pass filter with the center wavelength of 532 nm and a ND16 filter were coupled together in front of the CMOS camera to make the keyhole area more distinguishable against the other parts of the weld pool.

Fig. 3 Static radial basis function neural network model for keyhole dynamics

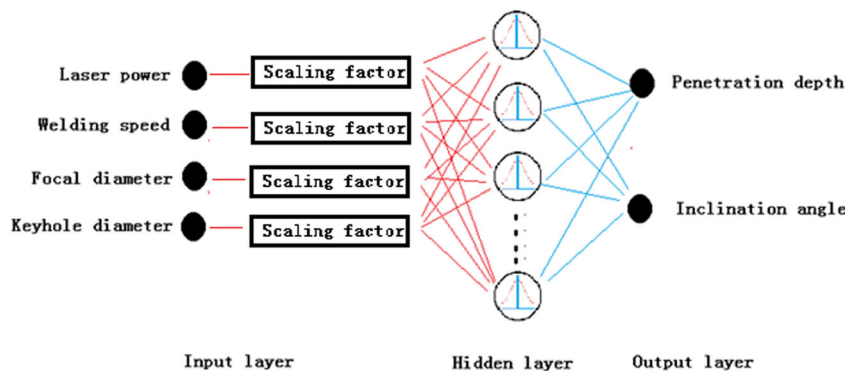
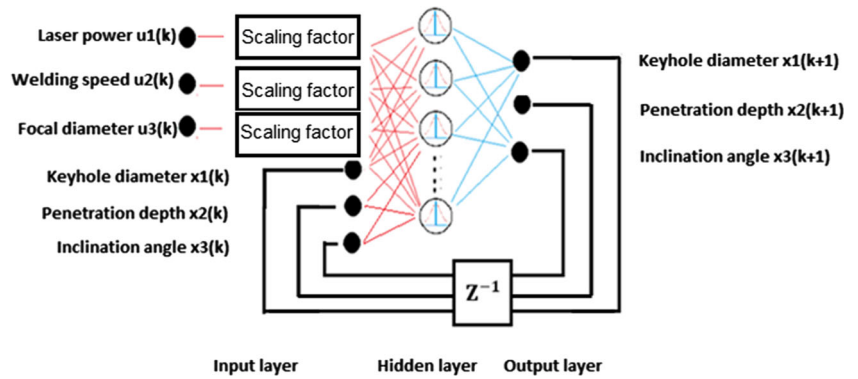


Fig. 4 Dynamic radial basis function neural network model for keyhole dynamics



3 Methodology of estimating keyhole dynamics

Keyhole dynamics is very important in the keyhole welding process because it can directly impact welding quality. However, an accurate mathematical model that could depict the keyhole dynamics is not readily available and also would be difficult to use for real-time applications. Thus, in this section, the application of a radial basis function neural network is introduced to identify the keyhole dynamics.

3.1 Radial basis function neural network

In system identification, a neural network is used to approximate an unknown system. In this study, a radial basis function neural network is selected to approximate the keyhole dynamics. The output of RBFNN is a linear combination of radial basis functions of the inputs and neuron parameters [24].

Given a continuous function $F: R^+ \rightarrow R$, and points $\{X_j^c; j=1, \dots, p\}$, $X_j^c \in R^+$, the function F can be defined using radial basis functions as [24] follows:

$$t_p(X) = \sum_{j=1}^p \lambda_j^p \Phi(|X - X_j^c|) + \lambda_0^T X \tag{1}$$

where $|\cdot|$ is the Euclidean norm. $\Phi(\cdot)$ is the radial basis function whose value depends only on the distance from the origin. X is the input vector. The vector X_j^c contains the centers of the basis function, which are determined by the training algorithm. The parameters λ_j^p are the weights between the nodes of basis function and output layer, and λ_0^T is the weight for the linear term. The value p is the number of basis functions in the

neural network. The goal of using RBFNN is to reduce the errors between $F(X)$ and $t_p(X)$ by choosing the proper coefficients of λ_j^p and λ_0^T .

3.2 Static RBFNN for keyhole dynamics

In order to generate a dynamic RBFNN to approximate keyhole dynamics in the transient state of keyhole welding, a static RBFNN is first developed to capture the correlation between welding parameters and keyhole geometric features. Because the welding speed range is from 1 to 4 m/min in this work, the detected keyhole boundary is quite similar to a circle. Thus, the keyhole diameter is used as a measurable keyhole feature. The inputs of the proposed static RBFNN include laser power, welding speed, and focal diameter, as well as keyhole diameter. The outputs consist of the penetration depth and keyhole front tilting angle. The schematic of the static RBFNN is shown in Fig. 3. The radial basis function used is

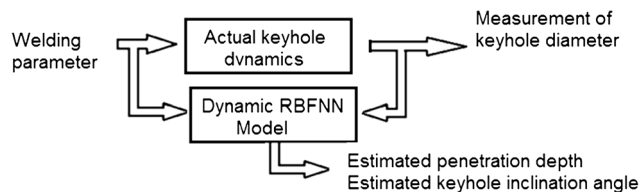


Fig. 5 Structure of estimator based on RBFNN

Table 3 Designed experiments

Experiment no.	Laser power (W)	Welding speed (m/min)
1	400	1
2	400	2
3	400	3
4	400	4
5	600	1
6	600	2
7	600	3
8	600	4
9	800	1
10	800	2
11	800	3
12	800	4
13	1000	1
14	1000	2
15	1000	3
16	1000	4

the Gaussian function, as shown in Eqs. (2) and (3). X and X_j^c have been defined in Section 3.1.

$$\Phi(r) = \exp(-r^2) \tag{2}$$

$$r = |X - X_j^c| \tag{3}$$

The noteworthy point of the static RBFNN in Fig. 3 is the scaling factor between the input data and hidden neurons. To guarantee the accuracy of the neural network, the scaling factors are utilized to map all the inputs to the same range, from 0 to 1. Considering the upper limit of the laser power as 1000 W and the maximum welding speed used as 4 m/min, the scaling factors for laser power, welding speed, focal diameter, and keyhole diameter are respectively 0.001, 0.1, 0.001, and 1. The orthogonal least square genetic algorithm (OLSGA) [26] is adopted to train this static RBFNN.

3.3 Dynamic RBFNN for keyhole dynamic estimation

In the welding process, although the well-trained static RBFNN is able to approximate the penetration depth and keyhole inclination angle in steady state welding, the keyhole dynamics in transient state welding cannot be predicted. Therefore, a dynamic RBFNN model is proposed to approximate the keyhole dynamic process with three state variables: keyhole diameter, penetration depth, and keyhole inclination angle. Among these three, the keyhole diameter is a measurable state variable, but the other two are unmeasurable. The dynamic model is illustrated in Fig. 4. In this dynamic model, the input includes both the welding parameters and the past values of three state variables.

In modeling the dynamic system, the neural network approach is to generate an approximation through the input-output measurements. Once data is collected over a range of initial conditions for several experiments, the neural network must be trained to properly approximate the system dynamics. An unknown plant is described by:

$$x_{k+1} = f(x_k, u_k) + w_k \tag{4}$$

$$y_k = h(x_k) + v_k \tag{5}$$

where state vector x_k is n-dimensional and the output vector y_k is assumed to be as m-dimensional. State and measurement noise vectors w_k and v_k are assumed to be independent Gaussian white processes with zero mean. The RBFNN then approximates the plant dynamics for each experiment i as follows:

$$x_{k+1}^i = [\Lambda \quad \Lambda_0] \begin{bmatrix} \Psi(X_k^i) \\ X_k^i \end{bmatrix} + w_k^i \tag{6}$$

$$z_k^i = x_k^i + \zeta_k^i \tag{7}$$

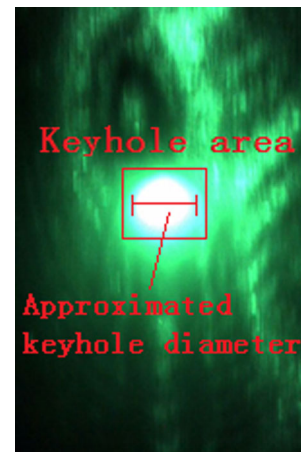


Fig. 6 Detected keyhole area and keyhole diameter

where X_k^i contains the state variables and the input for experiment i , and $\Psi(X_k^i) = [\Phi_1(X_k^i), \dots, \Phi_p(X_k^i)]^T$ contains the basis functions corresponding to p centers. Each row of the matrices Λ and Λ_0 correspond to an element of the approximated vector function $\hat{f}(\cdot)$. Since the parameters appear in the RBFNN as a linear form, least squares estimation is possible. The state estimator is designed for use with the RBFNN, and the gain matrix is derived on the basis of an upper bound covariance matrix. In addition, the consideration of approximation error in the estimation algorithm successfully minimizes filter divergence. The details of the training method and structure of dynamic observer are discussed completely in Elanayar and Shin [24].

For the keyhole dynamics, the structure of the dynamic estimator is shown in Fig. 5. The experiment number i is determined by the actual transient welding situations that are considered in the next section.

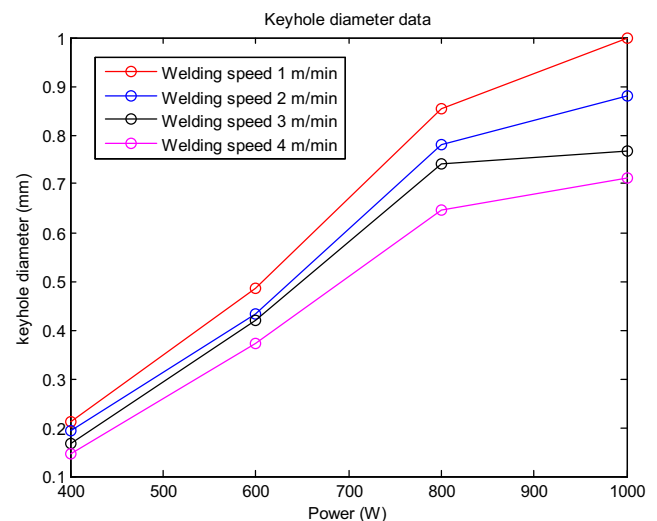
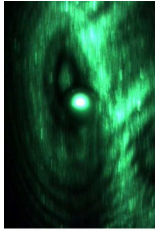
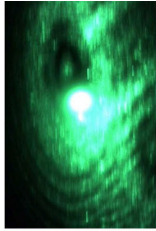
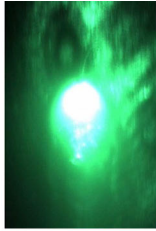
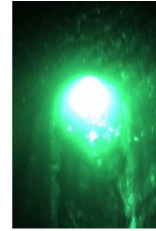
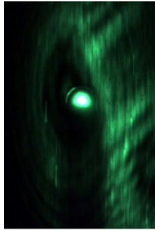
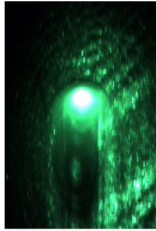
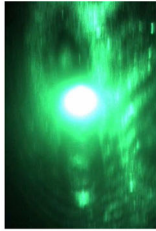
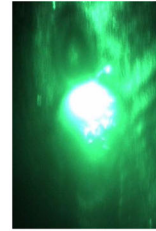
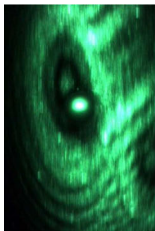
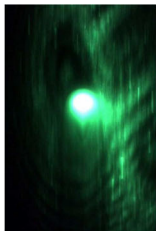

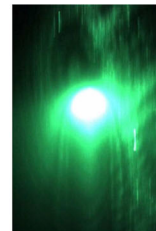
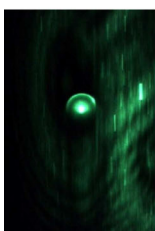
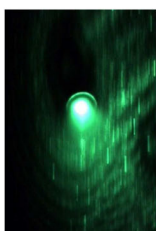

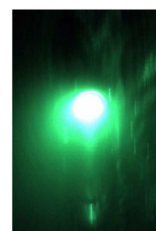


Fig. 7 Keyhole diameters under different welding parameters

Table 4 Average keyhole diameters from images: (150 pixels=1 mm)

	400 W	600 W	800 W	1000 W
1 m/min	32 (0.213mm) 	73 (0.486mm) 	128(0.853mm) 	150 (1mm) 
2 m/min	29 (0.193mm) 	65 (0.433mm) 	117 (0.78mm) 	132 (0.88mm) 
3 m/min	25 (0.167mm) 	63 (0.42mm) 	111 (0.74mm) 	115 (0.767mm) 
4 m/min	22 (0.147mm) 	56 (0.373mm) 	97 (0.647mm) 	107 (0.713mm) 

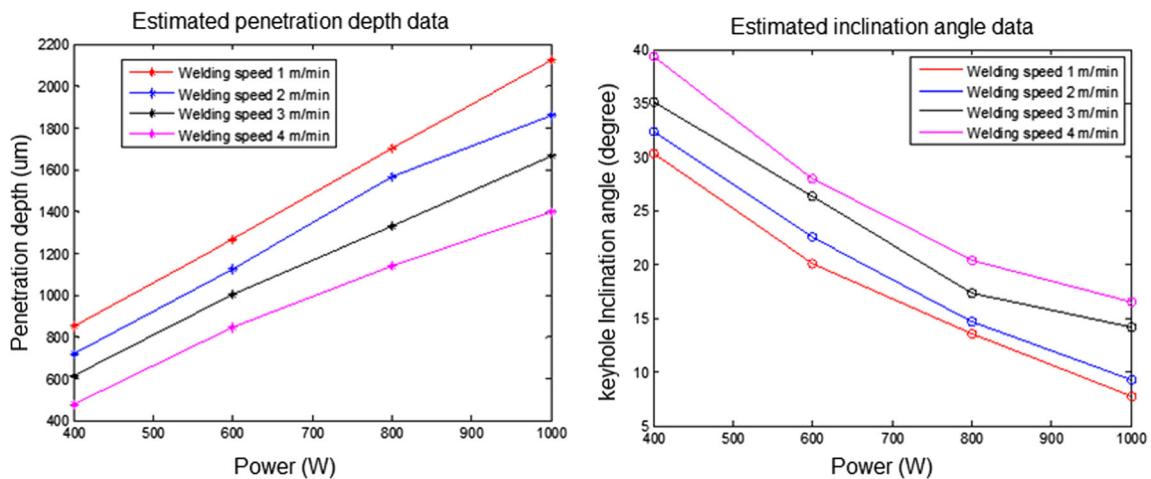


Fig. 8 Experimental data for penetration depth (left) and inclination angle (right)

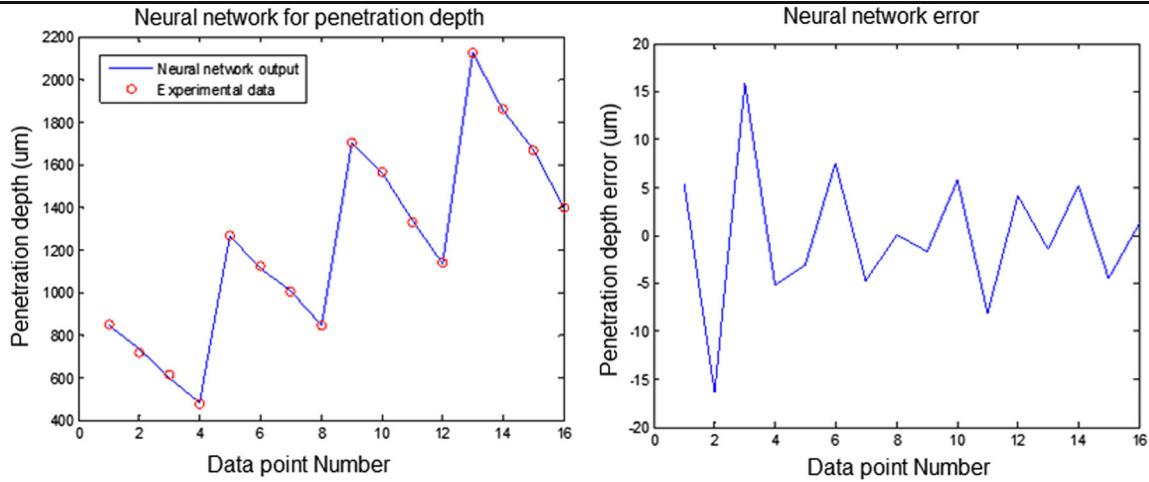


Fig. 9 Training results and errors of penetration depth

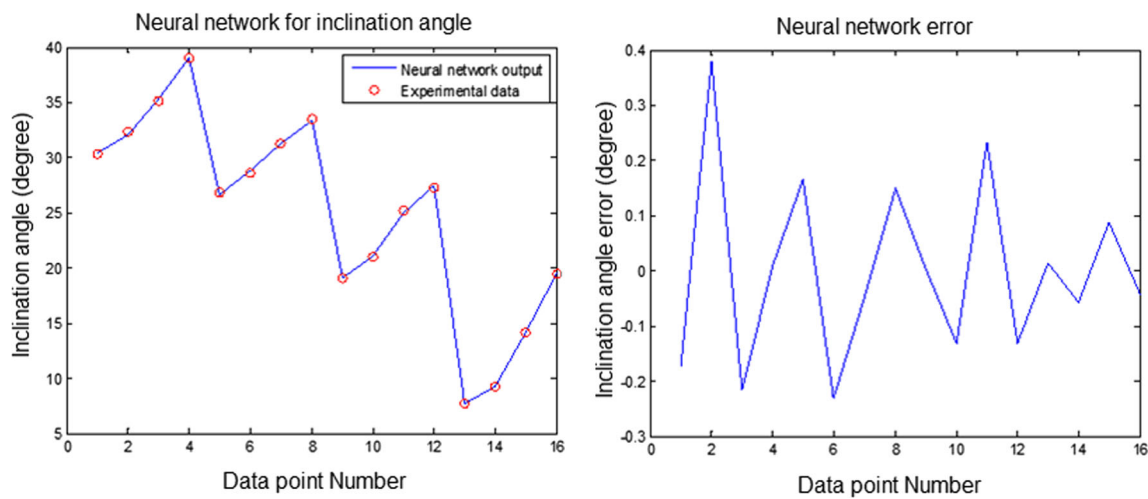


Fig. 10 Training results and errors of inclination angle

4 Results and analysis

4.1 Data collection of static RBFNN

Since the training of static RBFNN is based on the input and output data, experiments are necessary to collect the data for training the neural network. In consideration of the range of interest for welding parameters, the experiments are designed as shown in Table 3. The focal diameter of the laser equipment is kept at 200 µm, so it is not listed in Table 3 but should still

Table 5 Test data for penetration depth

Power (W)	Welding speed (m/min)	Focal diameter (µm)	Keyhole diameter (mm)	Experimental keyhole depth (µm)	Neural network keyhole depth (µm)
500	2	200	0.35	981	1007.0
500	3	200	0.324	889	866.2
500	4	200	0.27	687	674.32

be regarded as an input for the expandability of the proposed RBFNN.

4.1.1 Detected keyhole diameters

The keyhole diameters are detected by the coaxial monitoring system, as shown in Fig. 6. The average values of keyhole diameters under different welding parameters are plotted in Fig. 7, and the corresponding captured images are summarized in Table 4. As can be seen, the change of keyhole size is not quite linear with respect to the change of welding

Table 6 Test data for inclination angle

Power (W)	Welding speed (m/min)	Focal diameter (µm)	Keyhole diameter (mm)	Experimental inclination angle (°)	Neural network inclination angle (°)
500	2	200	0.35	30.6	31.86
500	4	200	0.27	35.5	36.57

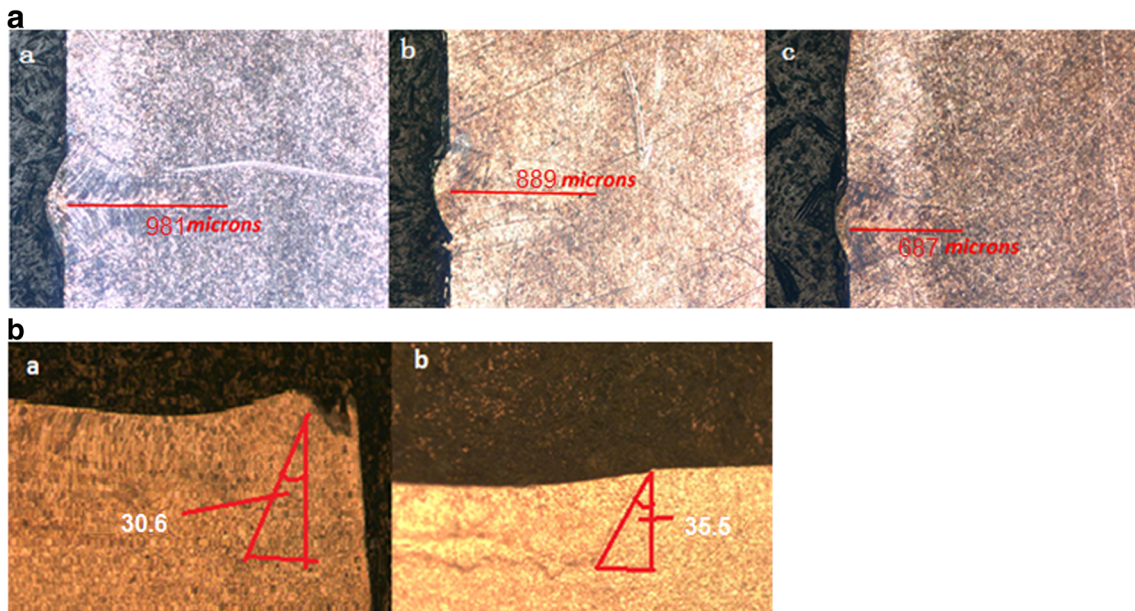


Fig. 11 **A** Penetration depth of *a* 500 W, 2 m/min; *b* 500 W, 3 m/min; and *c* 500 W, 4 m/min. **B** Inclination angle of *a* 500 W, 2 m/min and *b* 500 W, 4 m/min

condition. Generally, an increase in laser power or a decrease in welding speed makes the keyhole size larger.

4.1.2 Penetration depth and inclination angle

The techniques for measuring penetration depth and inclination angle are different since both of them cannot be directly measured from the coaxial monitoring system. Therefore, the cross section view of the post-processed weld is used to realize the data collection. The cross section view perpendicular to the weld provides sufficient information on the penetration depth. As for the inclination angle, the weld section was cut along the symmetrical central line in the welding direction. The longitudinal cross section view shows the angle clearly at the end of each weld. All the cross sections were ground, polished, and etched in order to reveal the clear welding

profile. The experimental data for the penetration depth and inclination angle are plotted in Fig. 8.

4.1.3 Training results of static RBFNN

To conduct off-line training, OLSGA [26] is utilized since it can better approximate the system features even the data set is insufficient. The training result for penetration depth is shown in Fig. 9, while the training result for inclination angle is shown in Fig. 10. From the error plots, it can be seen that both errors are very small, less than 1 %, when compared to the actual data sets.

4.1.4 Testing of neural network

The well-trained static neural network covers the range of welding power from 400 to 1000 W and the welding speed

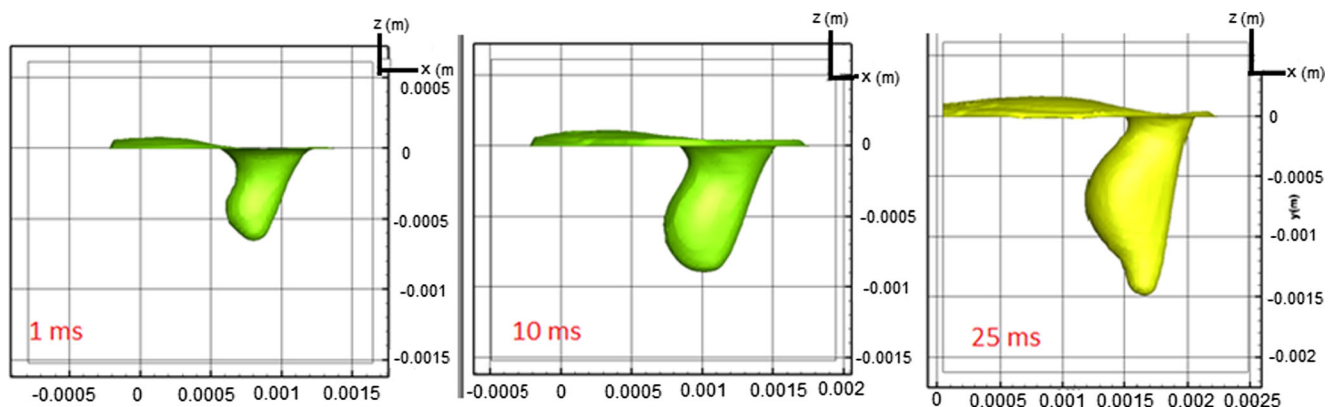


Fig. 12 Training data from numerical simulations (case of changing power)

from 1 to 4 m/min. To test the effectiveness of the static RBFNN, data other than the training sets are used. In this work, the test experiments are conducted with the laser power of 500 W and the welding speeds of 2, 3, and 4 m/min. The comparisons between the actual results and neural network approximation are summarized in Tables 5 and 6. The corresponding experimental results are also shown in Fig. 11A, B. When compared with the test results, the errors of the neural network are all less than 3 %, which means this static neural network can be utilized to approximate correlations between

the different welding parameters and keyhole geometries in the steady state welding process.

4.2 Dynamic RBFNN-based observer for keyhole dynamic estimation

4.2.1 Data training of dynamic RBFNN

As for the dynamic laser welding process, the keyhole geometry is estimated based on the dynamic RBFNN shown in

Fig. 13 **a** Dynamic neural network training results for changing laser power. **b** Dynamic neural network training results for changing welding speed

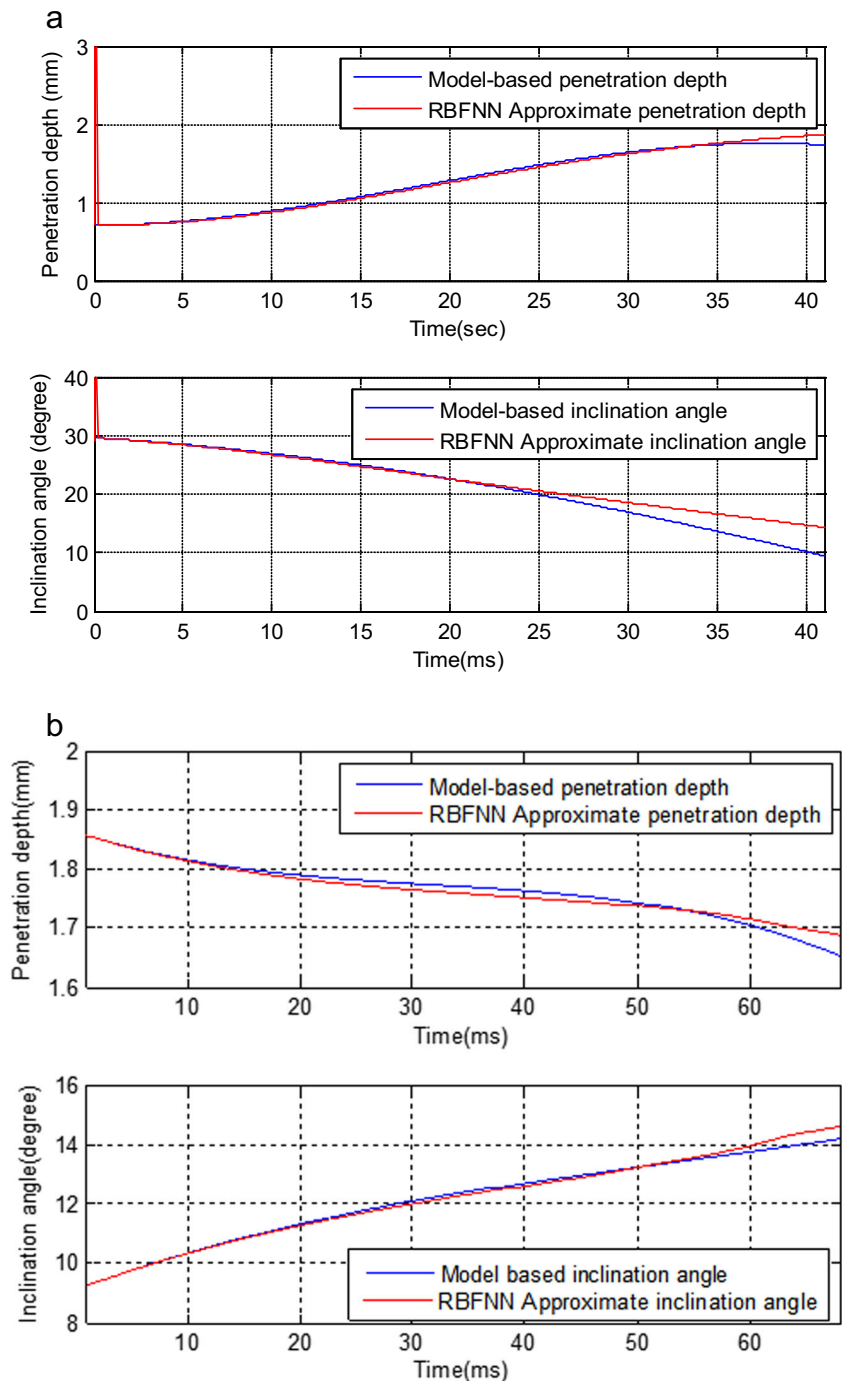


Fig. 4. In this work, two groups of experiments are carried out for transient state laser welding. The first one suddenly changes laser power from 400 to 1000 W (changing time is less than 1 ms) with a constant welding speed of 2 m/min. The second changes the welding speed from 2 to 3 m/min with a constant acceleration rate of 15 m/s² and laser power of 1000 W. The focal diameter used in the experiments is still 200 μm. To train the dynamic neural network model, the transient data is obtained from the numerical model [8] with an output every 0.1 ms. Figure 12 shows the keyhole dynamic changes predicted by this numeric model with respect to time. The entire transient state process lasts 41 and 68 ms for the first and second case, respectively. The training results of the dynamic neural network are shown in Fig. 13a, b. It is obvious that the trained RBFNN is capable of capturing the keyhole dynamics very well.

4.2.2 Estimation results of dynamic RBFNN observer

After the training, the observer is used to estimate the penetration depth and inclination angle. The actual penetration depth from the cross section view along the centerline of the weld is compared with the estimated keyhole penetration depth. As shown in Fig. 14, the red circles of the actual

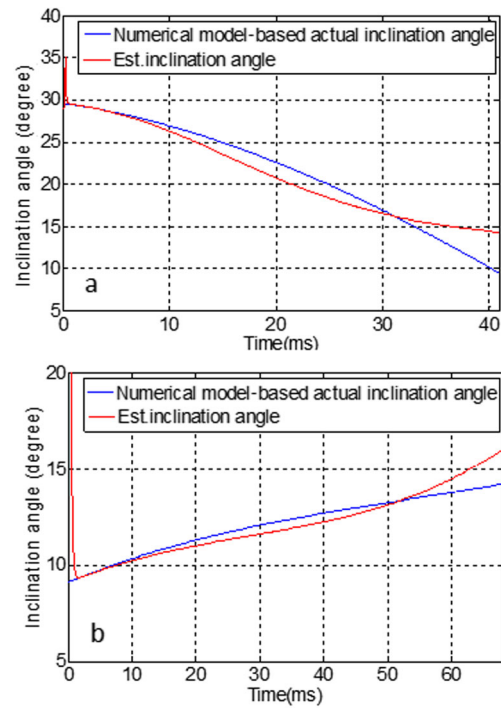


Fig. 15 Comparison of numerical model-based actual angle and estimated angle. a Changing power and b changing speed

Fig. 14 Comparison of estimated penetration depth and experimental results for a changing power and b changing speed

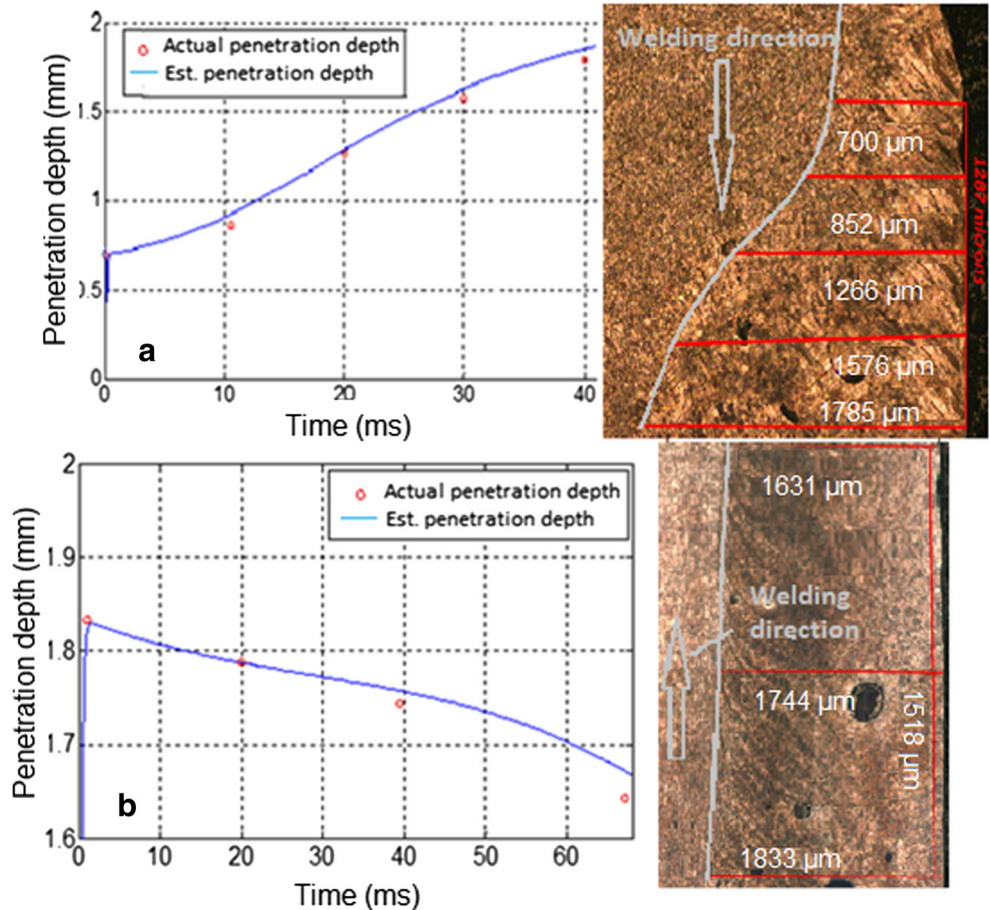
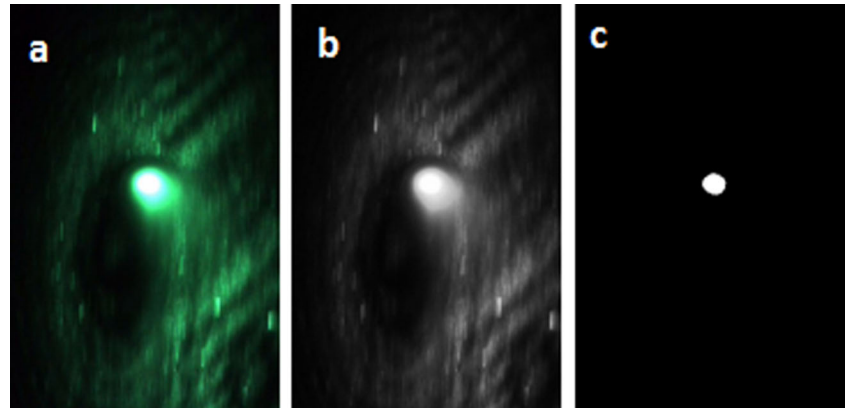


Table 7 Chemical composition of magnesium alloy AZ31B

Element	Al	Zn	Mn	Si	Cu	Ca	Fe	Ni	Mg
Portion (%)	2.5–3.5	0.7–1.3	0.2	0.05	0.05	0.04	0.005	0.005	Balance

Fig. 16 Keyhole area detection with stainless steel. **a** Original image, **b** converted gray image, and **c** binarized image

penetration depth are located very close to the blue line of estimated penetration depth. As for the keyhole inclination angle, the estimated results are compared to the actual model-based data in Fig. 15, in which predicted inclination angle acceptably represents the actual experimental result. These results demonstrate the accuracy of keyhole dynamic estimation via the RBFNN-based observer.

4.3 Porosity prediction

To predict the potential porosity and evaluate the welding quality, two approaches with the coaxial monitoring system are proposed, one of which is based on the predefined bound of variation and the other derived from the statistical analysis. As can be seen in the experimental results, the detected keyhole size has fluctuations even in the steady state of welding. Under certain welding conditions, variations of the keyhole size exceed the preset range due to the possibility of a

collapsed keyhole and porosities formed inside the weld pool. Through analyzing these imaging signals, welding porosities could be predicted in real time for both stainless steel 304 and magnesium alloy AZ31B (the composition is shown in Table 7).

- (1) Image binarization: After capturing the images of the keyhole, the color images are converted to gray ones, which consist of all pixels with the grayness value from 0 to 255. For the welding of stainless steel, the brightest part of the captured image is the keyhole area. The threshold value for image binarization is chosen as 240. Thus, pixels with grayness value under 240 are reset to 0, while values above 240 are reset to 255, as shown in Fig. 16. However, due to the difference of the absorptivity ratio of the green light, the keyhole for magnesium is darker than its surroundings, as marked out by red squares in Fig. 17. The threshold value for image binarization of magnesium welding is chosen as 80 in the

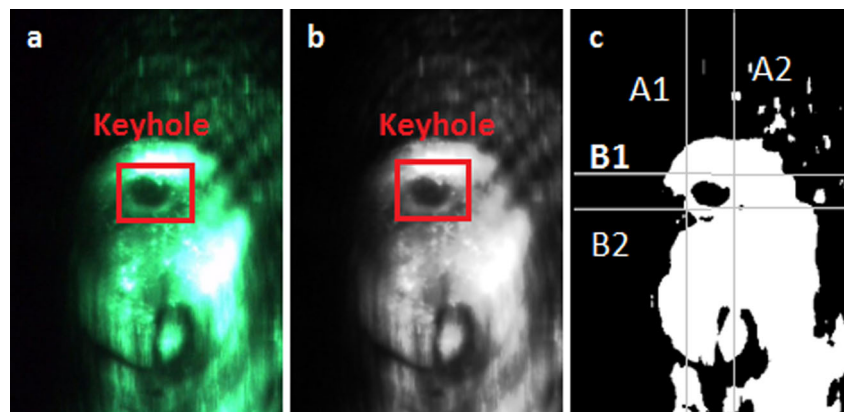
Fig. 17 Keyhole area detection with magnesium alloy. **a** Original image, **b** converted gray image, and **c** binarized image

Table 8 Designed experiment parameters for stainless steel

Experiment no.	Laser power (W)	Welding speed (m/min)	Welding quality
1	1000	1	Poor
2	1000	2	Poor
3	500	2	Good

Table 9 Designed experiment parameters for magnesium alloy

Experiment no.	Laser power (W)	Welding speed (m/min)	Welding quality
1	700	0.9	Good
2	800	2	Poor
3	900	2	Poor

present work. The converted image and binarization results are shown in Fig. 17.

- (2) Keyhole size determination: To describe the keyhole size, the total pixel number of the keyhole area is used. For stainless steel, the binarization is able to clearly separate the keyhole from the background, and thus, the pixel number N with grayness value of 255 is regarded as the size of the keyhole area. On the other hand, some additional locating techniques are necessary due to the noises of binarized magnesium images. The relative position of the keyhole center in an entire captured image is fixed since the monitoring system cannot be moved during the welding process; consequently, only the region bounded by lines A1, A2, B1, and B2 is considered, as shown in Fig. 17c. From the actual experimental results, it is confirmed that no keyhole area is larger than this bounded region. The total pixel number with grayness value of 0 inside this predefined search area is used to determine the keyhole size as N .
- (3) Mean value, upper and lower bound: After recording a series of keyhole images that contain K consecutive frames, the mean value of the keyhole size is determined as $M = \frac{1}{K} \sum_{i=1}^K N_i$. In the experiment with stainless steel, the fluctuation below the 10 % is taken as a reasonable change of the keyhole size and hence the upper and lower bounds are defined as 1.1 and 0.9 M , respectively. When considering the more unstable properties of the

magnesium alloy, fluctuation of keyhole size around the mean value less than 25 % is assumed to be a reasonable change. Consequently, the upper and lower bounds for magnesium alloy are, respectively, 1.25 and 0.75 M .

- (4) Experiment design for welding quality classification: In the experiment design, different welding parameters are selected for resultant welds classified as either good welding or poor welding. The designed welding parameters are listed in Tables 8 and 9. Through the cross-sectional views of the post-processed welds, as illustrated in Figs. 18 and 19, the corresponding welding quality is also determined.
- (5) Porosity prediction method 1: If there are calculated keyhole sizes located out of the lower and upper bounds, it means that the unusual keyhole changes happened in the welding process and there is a high chance of porosity formation in the base material. In Figs. 20a,b and 21b, c, either many points are outside the predefined regions or sharp peaks occur in the plots, where the undesired points are all marked by red dots. On the other hand, all of the points are within the two bounds in Figs. 20c and 21a, which means that few welding defects are detected during the welding process. Therefore, the detected results from Figs. 20 and 21 accurately reflect the welding qualities summarized in Tables 8 and 9.
- (6) Porosity prediction method 2: As the variation of the keyhole size is a statistical process, the relative standard

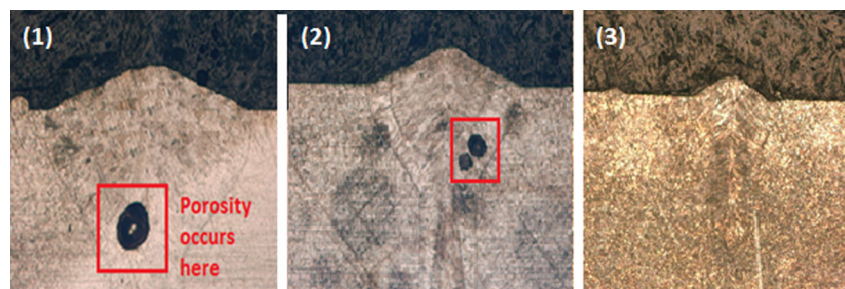
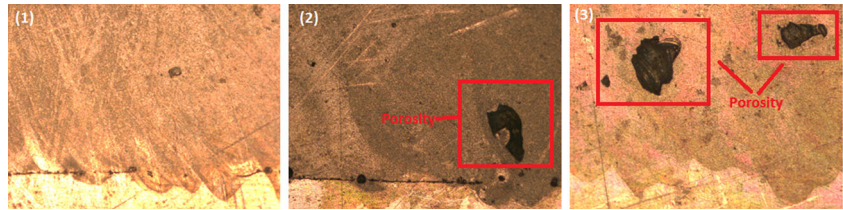
Fig. 18 Horizontal cross section view of weld on stainless steel

Fig. 19 Longitudinal cross section view of weld on magnesium



error (RSE) can be applied to get a more qualitative measure of the variance around the mean in estimating the welding quality, where $RSE = \frac{\sigma(\text{Standard deviation})}{M(\text{Mean value})}$. For the case in Fig. 20, $RSE_1=0.1006$ for the first one, $RSE_2=0.0633$ for the second one, and $RSE_3=0.0377$ for the third one. For the magnesium alloy in Fig. 21, $RSE_1=0.1079$ for the first one, $RSE_2=0.2657$ for the second one, and $RSE_3=0.213$ for the third one.

Apparently, the measurements with lower RSE indicate that the welding process is likely to run smoothly with less porosities. Based on experimental results, the “good welding” could be regarded as welding with RSE less than 0.05 for stainless steel and less than 0.15 for magnesium alloys.

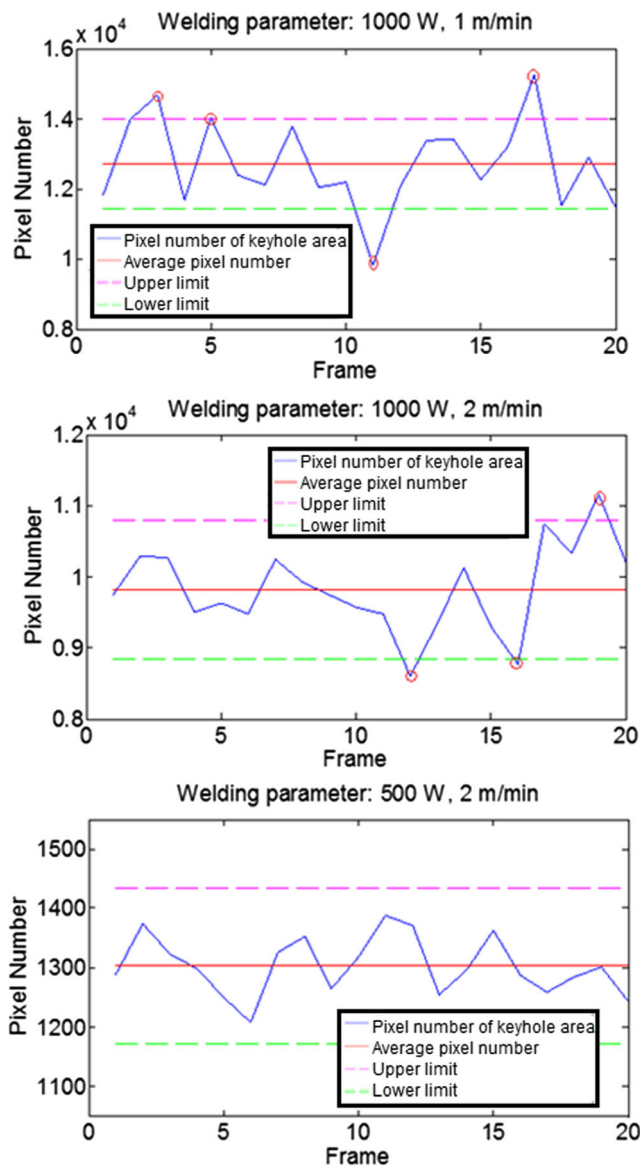


Fig. 20 Detected keyhole sizes with stainless steel

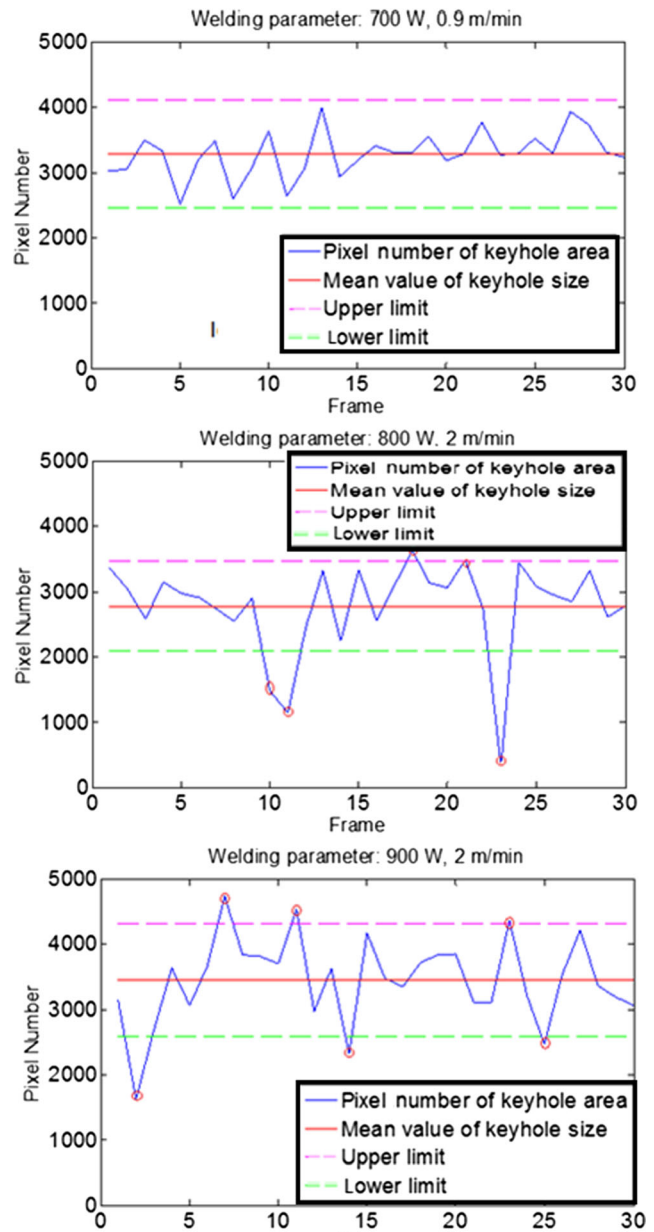


Fig. 21 Detected keyhole sizes with magnesium alloy

5 Conclusion

In the keyhole welding process, keyhole dynamics significantly influence welding quality. The proposed static radial basis function neural network provides an accurate prediction of the major keyhole features based on the welding conditions and measurements by the coaxial monitoring system. Under the changing welding parameters, the dynamic radial basis function neural network observer performs well in estimating the penetration depth and inclination angle. Additionally, the proposed approaches of porosity prediction based on the visual monitoring system successfully indicate the occurrence of potential porosities in real-time experimentation.

References

- Matsunawa A, Semak V (1997) The simulation of front keyhole wall dynamics during laser welding. *J Phys D Appl Phys* 30:798–809
- Lankalapalli KN, Tu JF, Gartner M (1996) Model for estimating penetration depth of laser welding processes. *J Phys D Appl Phys* 29:1831–1841
- Ronda J, Siwek A (2011) Modelling of laser welding process in the phase of keyhole formation. *Arch Civ Mech Eng* 113:739–752
- Ki H, Mohanty PS, Mazumder J (2002) Modeling of laser keyhole welding: part I. Mathematical modeling, numerical methodology, role of recoil pressure, multiple reflections, and free surface evolution. *Metall Mater Trans* 33A:1817–1830
- Ki H, Mohanty PS, Mazumder J (2002) Modeling of laser keyhole welding: part II. Simulation of keyhole evolution, velocity, temperature profile, and experimental verification. *Metall Mater Trans* 33A:1831–1842
- Pang S, Chen L, Zhou J, Yin Y, Chen T (2011) A three-dimensional sharp interface model for self-consistent keyhole and weld pool dynamics in deep penetration laser welding. *J Phys D Appl Phys* 44:025301
- Zhao H, Niu W, Zhang B, Lei Y, Kodama M, Ishide T (2011) Modelling of keyhole dynamics and porosity formation considering the adaptive keyhole shape and three phase coupling during deep-penetration laser welding. *J Phys D Appl Phys* 44:485302
- Tan W, Bailey NS, Shin YC (2013) Investigation of keyhole plume and molten pool based on a three-dimensional dynamic model with sharp interface formulation. *J Phys D Appl Phys* 46:055501
- Li L (2002) A comparative study of ultrasound emission characteristics in laser processing. *Appl Surf Sci* 186:604–610
- Wang J, Yu H, Qian Y, Yang R (2011) Interference analysis of infrared temperature measurement in hybrid welding. Tarn TJ et al. (Eds.): *Robotic welding, intelligence and automation*; LNEE 88:369–74
- Huang RS, Liu LM, Song G (2007) Infrared temperature measurement and interference analysis of magnesium alloys in hybrid laser-TIG welding process. *Mater Sci Eng* 447:239–243
- Saeed G, Lou M, Zhang YM (2004) Computation of 3D weld pool surface from the slope field and point tracking of laser beams. *Meas Sci Technol* 15:389–403
- Song HS, Zhang YM (2007) Three-dimensional reconstruction of specular surface for a gas tungsten arc weld pool. *Meas Sci Technol* 18:3751–3767
- Kim C, Ah D (2012) Coaxial monitoring of keyhole during Yb:YAG laser welding. *Opt Laser Technol* 44:1874–1880
- Zhang Y, Zhang C, Tan L, Li S (2013) Coaxial monitoring of the fiber laser lap welding of Zn-coated steel sheets using an auxiliary illuminant. *Opt Laser Technol* 50:167–175
- Fabbro R (2010) Melt pool and keyhole behaviour analysis for deep penetration laser welding. *J Phys D Appl Phys* 43:445501
- Fabbro R, Slimani S, Coste F, Briand F (2005) Study of keyhole behavior for full penetration Nd–Yag CW laser welding. *J Phys D Appl Phys* 38:1881–1887
- Fabbro R, Slimani S, Doudet I, Coste F, Briand F (2006) Experimental study of the dynamical coupling between the induced vapor plume and the melt pool for Nd–Yag laser welding. *J Phys D Appl Phys* 39:394–400
- Kawahito Y, Mizutani M, Katayama S (2007) Investigation of high-power fiber laser welding phenomena of stainless steel. *Trans JWRI* 362:11–16
- Wahba M, Katayama S (2012) Laser welding of magnesium alloys. *Trans JWRI* 411:11–23
- Katayama S, Mizutani M, Matsunawa A (2003) Development of porosity prevention procedures during laser welding. *Proc SPIE* 4831:281–288
- Seto N, Katayama S, Matsunawa A (2000) High-speed simultaneous observation of plasma and keyhole behavior during high power CO₂ laser welding: effect of shielding gas on porosity formation. *J Laser Appl* 12:245–250
- Kaplan AFH, Mizutani M, Matsunawa A, Katayama S (2002) Unbounded keyhole collapse and bubble formation during pulsed laser interaction with liquid zinc. *J Phys D Appl Phys* 35:1218–1228
- Elanayar S, Shin YC (1994) Radial basis function neural network for approximation and estimation of nonlinear stochastic dynamic systems. *IEEE Trans Neural Netw* 54:594–603
- Elanayar S, Shin YC (1995) Robust tool wear estimation with radial basis function neural networks. *Trans. of the ASME, J Dyn Control Syst* 117:459–67
- Lee CW, Shin YC (2003) Construction of fuzzy systems using least-squares method and genetic algorithm. *Fuzzy Sets Syst* 137:297–323